

Validation of AVHRR and MODIS ice surface temperature products using in situ radiometers

Ted A. SCAMBOS,¹ Terry M. HARAN,¹ Robert MASSOM²

¹National Snow and Ice Data Center, CIRES, University of Colorado, Boulder, CO 80309-0449, USA
E-mail: teds@icehouse.colorado.edu

²Department of the Environment and Heritage, Australian Antarctic Division and Antarctic Climate and Ecosystems CRC, University of Tasmania, Hobart, Tasmania 7001, Australia

ABSTRACT. Ship-borne and airborne infrared radiometric measurements during the ARISE cruise of September–October 2003 permitted in situ validation studies of two satellite-based ice surface skin temperature algorithms: the AVHRR Polar Pathfinder Ice Surface Temperature and the MODIS Sea Ice Surface Temperature. Observations of sea ice from the *Aurora Australis* ship's rail using a KT-19.82 radiometer were conducted between 25 September and 21 October during clear-sky overflights by AVHRR (41 passes) and MODIS (17 passes) on their respective satellite platforms. Data from both sensors show highly linear fits to 1 min integrated radiometer spot measurements, spanning the range 245–270 K with a $\pm 1.4^\circ\text{C}$, 1σ (AVHRR) and $\pm 1.0^\circ\text{C}$ (MODIS) variation relative to a 1:1 relationship. There was no significant offset. Helicopter observations made with a KT-19.85 radiometer on three dates (8, 19 and 20 October) provided more data (236 gridcell sites total), but over a more limited sea-ice skin temperature range (252–268 K), with higher variation ($\pm 1.7^\circ\text{C}$, 1σ) due to mixed-pixel issues. Comparison of MODIS and AVHRR algorithms directly, with both images acquired during a helicopter flight, indicates very high correlation and near-unity slope for the two satellite-based algorithms. Ship air-temperature data during the validation indicated moderate to strong inversions over sea ice under clear skies. These formed and decayed rapidly (tens of minutes) as clouds moved out of and into the zenith area.

INTRODUCTION

As the field of polar remote sensing turns increasingly from basic algorithm demonstration to change detection, the value of long-term calibrated and validated satellite datasets increases. Moreover, inter-calibration of datasets derived from different sensors becomes important as a means of extending the temporal record for detection of change. Here we link a 22 year record of ice surface skin temperature (1981–2003) derived from the Advanced Very High Resolution Radiometer (AVHRR) with a 6 year (2000–06), and growing, sea-ice temperature record produced from the Moderate-Resolution Imaging Spectroradiometer (MODIS).

The 22 year record of AVHRR ice temperature comes from the AVHRR 5 km and 1.25 km Polar Pathfinder Dataset, created and distributed by the US National Snow and Ice Data Center (NSIDC; Maslanik and others, 1997). The dataset spans the period 1981–2000 at 5 km, and 1993–2003 at 1.25 km (including archived Level 1B swath data at 1.1 km nadir resolution), and includes data from the US National Oceanic and Atmospheric Administration's NOAA-7, 9, 10, 11, 12, 14, 15 and 16 polar-orbiting satellite platforms. The MODIS-derived sea-ice surface temperature product (Sea Ice Extent 5 min swath 1 km product; Hall and others, 2004) is a 1 km Level 2 swath product of the Earth Observing System data product system. It is a cloud-masked dataset, available for both Terra and Aqua MODIS sensors for the period February 2000 (Terra) or July 2002 (Aqua) to the present (data products MOD29 and MYD29).

ARISE CRUISE

The Antarctic Remote Ice Sensing Experiment (ARISE) of September–October 2003 had as its mission the observation of Antarctic sea-ice characteristics, and the validation of a

number of remote-sensing-derived measurements over sea ice in Antarctic sea-ice conditions (Massom and others, 2006). This mission of the *Aurora Australis* used ship-board sensors, direct measurements and helicopter-mounted and -towed platforms to survey an extensive area of East Antarctic sea ice during spring conditions (Fig. 1). In addition to these ice surface temperature validation measurements, extensive calibration–validation studies were conducted to verify passive microwave-derived extent and concentration, visible/near-infrared albedo, thickness and snow-cover algorithms for sea-ice study. Algal system studies at the ice edge and throughout the Southern Ocean were also conducted.

SATELLITE SENSOR ICE SURFACE TEMPERATURE ALGORITHMS

Ice surface skin temperature is derived by measuring thermal-band emission (8–14 μm) from the snow surface (Key and Haefliger, 1992; Comiso, 1994; Lindsay and Rothrock, 1994). High emissivity of snow and a low atmospheric absorption in this range make this measurement feasible and relatively easy to calibrate. Both algorithms used here apply the split-window technique, based on

$$T_s = a + bT_{11} + c(T_{11} - T_{12}) + d[(T_{11} - T_{12})(\sec \theta - 1)],$$

where T_s is the measured skin emission temperature, a , b , c and d are constants derived from a regression of calibration data, θ is sensor scan angle through the atmosphere, and T_{11} and T_{12} are thermal channel brightness temperature measurements in the 11 and 12 μm range. For AVHRR, channels 4 (10.3–11.3 μm) and 5 (11.5–12.5 μm) are used; for MODIS, bands 31 (10.78–11.28 μm) and 32 (11.77–12.27 μm). Calibration data for the regression come from polar-region

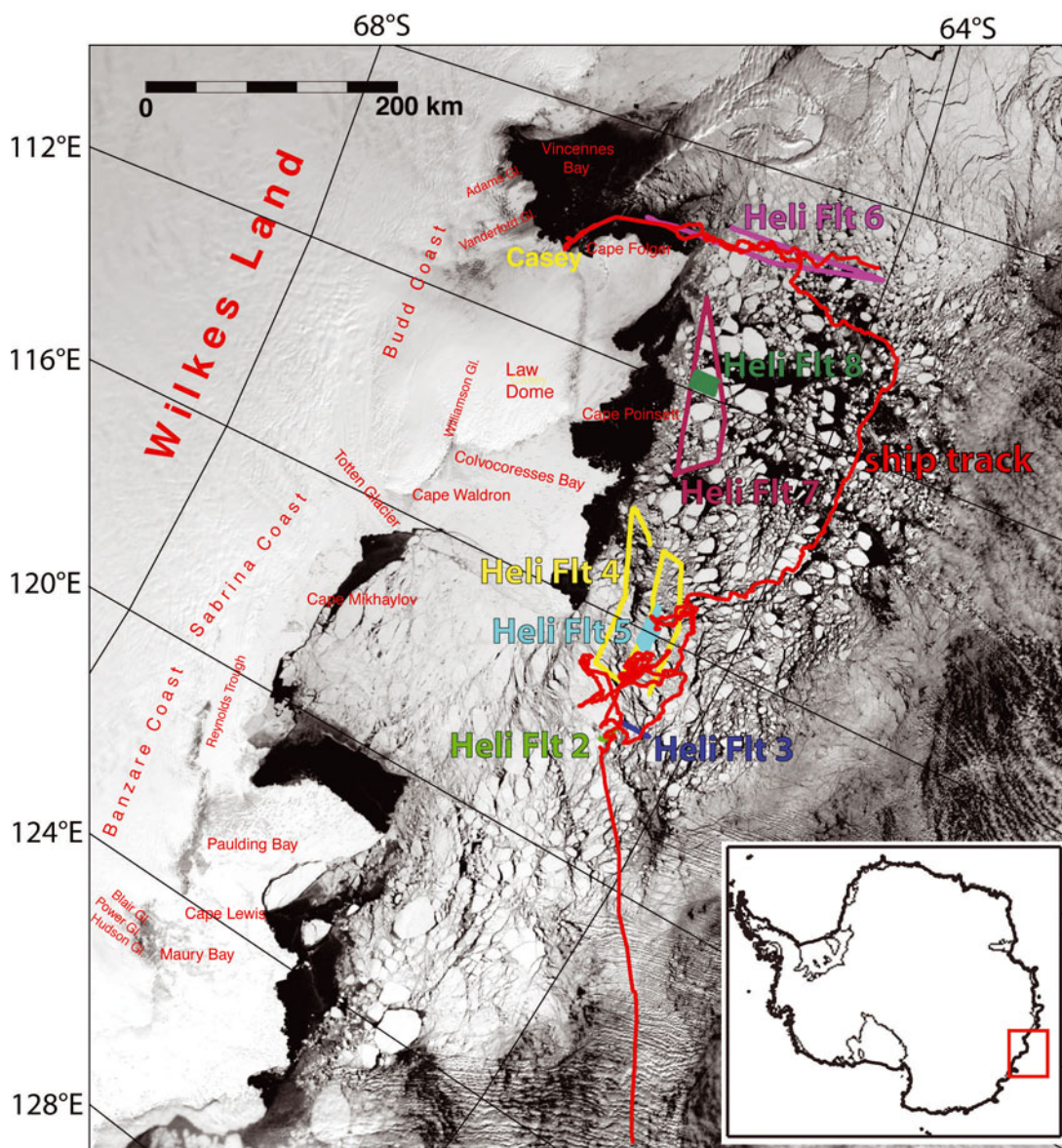


Fig. 1. Image map derived from a Terra MODIS image from 20 October 2003 (0135 UT acquisition time), showing the course of the ARISE cruise (red line) between 25 September and 21 October 2003, and tracks of helicopter flights with validation data ('Heli Flt' 2–8, various colors). 'Heli Flt 2' (green) was acquired on 3 October; 'Heli Flt 3' (blue) on 3 October; 'Heli Flt 4' (yellow) on 8 October; 'Heli Flt 5' (cyan) on 8 October; 'Heli Flt 6' (magenta) on 19 October; 'Heli Flt 7' (maroon) on 20 October; and 'Heli Flt 8' (dark green) on 20 October. The image shows sea-ice conditions (approximately) for only the last three helicopter flights.

radiosondes coupled with a radiative transfer model (LOW-TRAN; see Hall and others, 2004). For the AVHRR Polar Pathfinder dataset, the split-window approach is only possible with the AVHRR-3 sensor; the NOAA-10 sensor permits only a simpler algorithm using just channel 4 (AVHRR-2 sensor; see Hastings and Emery, 1992; Maslanik and others, 1997). AVHRR sensor series regression parameters are provided by Key and others (1997) and J. Key (personal communication, 2003). MODIS regression parameters are given in Riggs and others (1999; any updates to AVHRR or MODIS ice surface temperature parameters are available by request to NSIDC).

IN SITU MEASUREMENT METHODS AND COMPARISON WITH SATELLITE DATA

Validation of the two satellite-based temperature products was accomplished by comparing satellite-derived skin

temperatures in the regions surrounding the ship with in situ and airborne thermal radiometer measurements of the ice surface under clear-sky conditions. Two radiometers were used: a rail-mounted sensor imaging an area adjacent to the ship; and a similar device mounted to a nadir viewport on a helicopter (Fig. 2).

Rail-mounted system

The thermal radiometer used for the rail was a Heitronics KT-19.82, measuring the spectral range 8–14 μm . The device was mounted to the port side rail and pointed at the ice (or water) surface adjacent to the ship at a surface viewing angle of 60–30° below the horizon, with 30° as the nominal value. Several tests of sensitivity to viewing angle (over the range 60–15°) showed brightness temperature variations of just several tenths of a kelvin, with usually lower temperatures at high incidence angles, but variable. The 30° viewing angle was selected to place the viewing area well to one side of

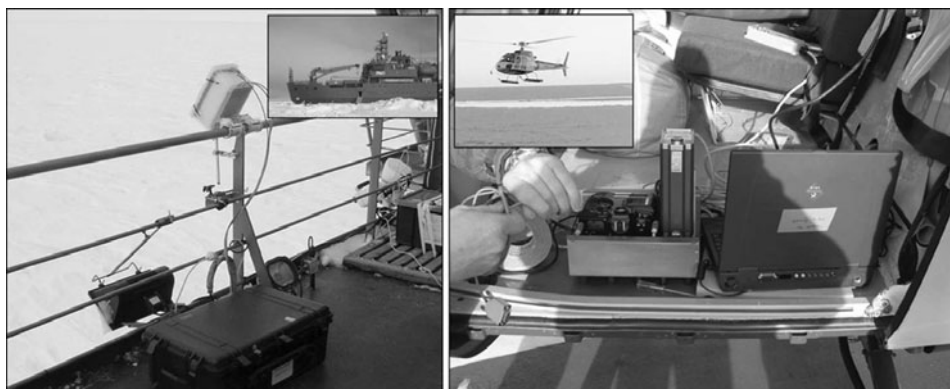


Fig. 2. Photographic collage illustrating in situ KT-19 radiometer measurement helicopter (right) and ship's-rail (left) configurations.

the ship, minimizing the effects of ship splash and fresh fractures while underway. Spot measurement area is roughly 0.5 m across, given the rail height of 15 m, the field of view of the instrument, and the 30° viewing angle. The radiometer was set in a foam-insulated box, and a self-regulating resistance heating system was installed to keep the instrument temperature at 280 ± 3 K. A data rate of 1 s was used. The device recorded brightness temperatures in kelvins (i.e. assuming an emissivity of 1.0 for all surfaces). Sensitivity of the device (rms of a constant-temperature surface at 1 s integration) was reported by the manufacturer as being 0.1 K. The accuracy of the device was checked before and after most runs by viewing a fresh ice-water bath. With emissivity set to 1, under clear skies, this test consistently reported temperatures of 272.2–272.6 K (see below for later correction for emissivity). Data were acquired for continuous multi-hour periods, spanning several overflights of the NOAA-12, NOAA-15 and NOAA-16 satellites, and the Terra and Aqua satellites, during both day and night. Approximately 20 observing sessions were conducted over the period 25 September–21 October 2003 (Fig. 3).

After acquisition, data were averaged to 1 min intervals and compared with several additional parameters acquired during the cruise: global positioning system (GPS) position,

GPS-derived speed, ship's air temperature (21 m above the sea surface), solar incoming radiation (a further indicator of cloudiness), wind direction and speed, and data from another radiometer aboard, MAERI (Marine–Atmosphere Emitted Radiance Interferometer; see Kearns, 2000; Minnett and others, 2001). In addition to minute-averaged mean KT-19 sensed temperature, the minimum, maximum and standard deviation for the 60 s interval was recorded. MAERI data reported a skin temperature of the surface given an emissivity, ϵ , of 0.9627 (value appropriate for sea water; Kearns and others, 2000), averaged over 12 min.

Helicopter-mounted system

A Heitronics KT-19.85, sensing emissions over a 9–11 μm range, was mounted to a nadir-viewing rack on a helicopter and flown on three days (29 September, 8 and 20 October 2003) for several hours in the vicinity of the ship (Figs 1 and 2b; see also Massom and others, 2006, fig. 6). These data were acquired every 2 s. The radiometric resolution for the instrument at this rate is given by the manufacturer as ± 0.1 K. The altitude of the helicopter was ~ 1500 m (5000 ft). At this height, the spot viewing area is ~ 65 m diameter. The helicopter unit was not temperature-controlled, and internal temperatures varied from 275 to 295 K.

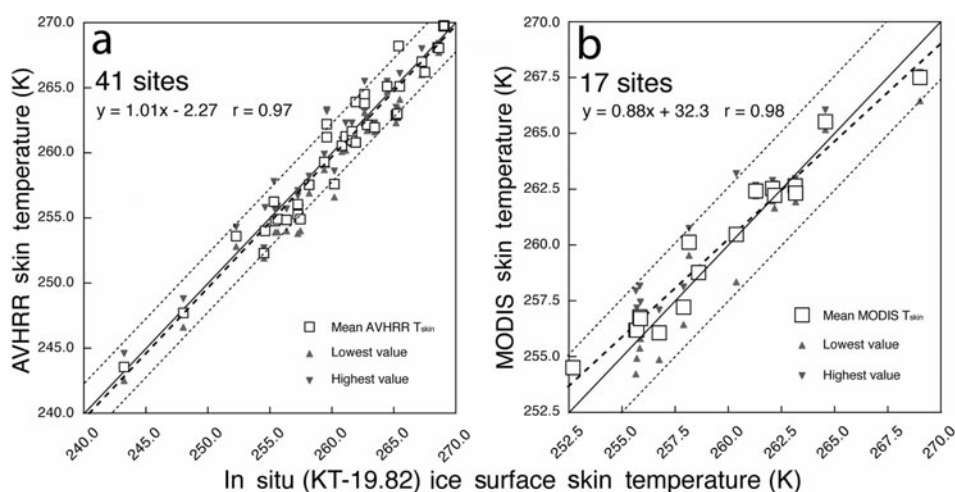


Fig. 3. Validation of AVHRR Polar Pathfinder ice surface temperature (a) and MODIS sea-ice surface temperature (b) using ship-rail-mounted KT-19.82 data. Ranges of image-grid pixel values at each calibration site shown by triangles above and below the mean value. Error of KT-19.82 measurement shown by width of box symbol (± 0.3 K). Best-fit line, with equation, shown for both sensors (thick dashed line); 1 : 1 line (solid), with lines at 2.5 K above and below the 1 : 1 reference (thin dotted lines) are also shown.

Emissivity correction

Emissivity corrections (e.g. correction from brightness temperatures to skin temperatures) were applied to the rail-mounted radiometry data by the following equation:

$$T_{\text{skin}} = \frac{T_{\text{BTice}} - [(1 - \varepsilon)(T_{\text{BTsky}})]}{\varepsilon},$$

where T_{skin} is the corrected ice surface skin temperature, T_{BTice} is the brightness temperature of ice, and T_{BTsky} is the mean all-sky brightness temperature. This follows a similar approach taken for the MAERI sensor in the measurement of ocean temperature (Kearns and others, 2000). In the sensitivity range of the rail-mounted KT-19.82 (8–14 μm), the mean spectral emissivity, ε , of snow/ice at a 30° surface incidence viewing angle is 0.985 (Dozier and Warren, 1982); it ranges from ~ 0.981 (15° incidence) to 0.997 as the viewing angle approaches vertical. With the 30° viewing angle for the rail-mounted system, it is necessary to correct for the 0.015 reflectivity factor, using an estimate of the clear-sky brightness temperature (direct measurements of clear sky by the KT-19 always fell below its sensitivity limit of ~ 220 K). We used 200 K for this value. For the helicopter-mounted KT-19.85, the sensitivity range (9–11 μm) has a mean ice emissivity that is higher at all incidence angles, and is 0.998 under nadir-viewing conditions (Dozier and Warren, 1982). Given this, and the uncertainty of the full-sky brightness temperature above the viewing point of the helicopter-mounted sensor, an ε value of 1.0 was used and no sky correction was applied.

Error of the KT-19 measurements

Noise levels for the KT-19.82 and KT-19.85 are noted above. In our in situ measurements, stationary observing periods for the KT-19.82 on the rail of the ship often showed long periods where variations were less than this, 0.05–0.07°C. With 1 min averaging, standard deviation during stationary viewing of uniform ice was typically 0.02–0.03°C. Given this, the main error source is presumed to be the sky correction. Our estimated all-sky brightness temperature of 200 K could vary by up to 20°C, depending on humidity and/or the presence of scattered or thin clouds. With a 20°C variation, the corrected KT-19 value shifts by 0.35 K, and we take this value as our likely error for the ship's-rail (KT-19.82) measurements. For the helicopter-mounted radiometer, the lack of a sky correction results in a $\sim 0.4^\circ\text{C}$ error, i.e. skin temperatures too cold by this amount assuming sky brightness temperatures of ~ 200 – 220 K.

Satellite images

Satellite data images from the AVHRR sensor on the NOAA-12, NOAA-15 and NOAA-16 satellites were down-linked as they flew overhead by the Terrascan system on *Aurora Australis*. The satellite data were processed using Polar Pathfinder algorithms identical to those used in the main NSIDC-based datasets for both albedo and ice surface temperature. These data were gridded to a 1.25 km grid in the Polar Pathfinder projection (Lambert Equal Area Polar Azimuthal). No cloud masking was applied; clear or cloudy sky conditions were determined by meteorological notes from aboard the ship, and examination of the albedo and thermal images. For the MODIS data, we requested MOD29 and MYD29 swath products for the same days that were shown to have large clear-sky areas in AVHRR, and for

which we had KT-19 measurements. These swath products were then gridded to the same Polar Pathfinder grid using the MODIS Swath to Grid Toolbox (MS2GT) software available from NSIDC.

Selection of validation points for the rail-mounted system

There were several factors considered in the selection of satellite-derived pixel values of skin temperature and mean KT-19 data for comparison. These are a result of the sub-gridcell spatial variability of the surface (sea ice and leads), the variation of temperature over time, and the movement of the ship through thick or thin ice. The ship, which typically followed open-water or light-nilas covered leads, was often on a boundary in temperature represented by a mixed-surface pixel in the gridded images. For this reason, nearby pixels, covering areas that were interpreted to be homogeneous at the 1.25 km scale, were used for comparison with the rail-mounted KT-19 temperatures. Moreover, the geo-registration of the AVHRR data using only the satellite ephemeris (conducted on board) results in geolocation errors of 3–7 km. These issues were avoided by selecting four to eight nearby gridcell pixels in regions of uniform brightness temperature (e.g. from large floes or uniform nilas/thin-ice areas) within a radius of ~ 15 km of the ship. The KT-19 measurements are selected from times close to (± 30 min) the acquisition times that represented periods when the port side of the ship saw a uniform surface type for several minutes. For example, if the measurement was over thick snow-covered ice floes, several nearby cold-floe areas from the images were compared with the coldest, lowest-variability minute-averaged measurements from the KT-19 record. For leads and polynyas (usually covered with thin grey to grey-white nilas) a similar approach was used, taking uniform but warmer temperatures from both the image data and KT-19 record. Open-water contamination was eliminated by selecting 60 mean points for which the maximum 1 s temperature was < 269 K. A similar approach was used for the MODIS–ship's-rail comparison, but here geo-referencing errors are within 50 m (Wolfe and others, 2002), and resolution is somewhat better (1.0 km), so comparison points could be kept within 5 km of the ship position.

Validation using the helicopter-mounted radiometer

Helicopter flights with remote-sensing data at the time of satellite overflights occurred on 8, 19 and 20 October 2003. Helicopter flights were typically 30 min to 3 hours in duration. We identified seven AVHRR and six MODIS scenes with acquisition times during the aerial radiometer collection.

The high resolution and extensive track length of the airborne radiometer requires that the satellite data be precisely geolocated, and that cloud areas are masked. To geolocate the AVHRR data, we shifted the image grids to a best-fit match with the closest MODIS image. Usually these scenes were within 1 hour of each other, minimizing the effect of sea-ice drift in the interval. We also used the MODIS cloud mask to eliminate cloud-impacted pixels and spots from the AVHRR and KT-19.85 profile data.

Figure 4 provides an example of the airborne radiometer data and near-simultaneous satellite data. As shown in Figure 4e, the airborne radiometer acquires a much higher-resolution profile than the satellites are capable of resolving. At the typical speed of flight of the helicopter ($\sim 40 \text{ m s}^{-1}$),

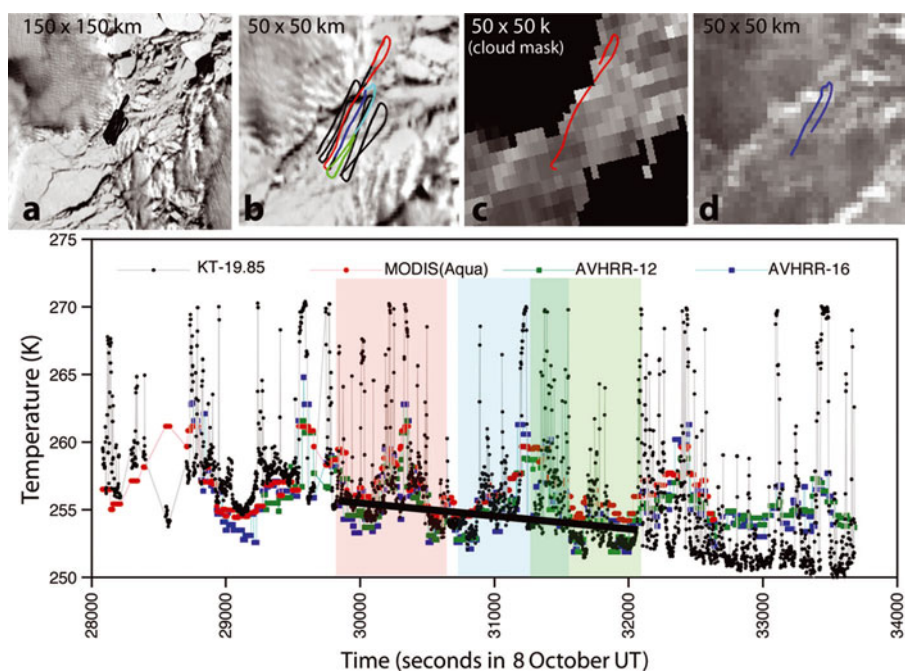


Fig. 4. Helicopter validation flight of 8 October. (a) Regional sea-ice extent and clouds shown in MODIS Channel 1 image (250 m pixel size) acquired during the flight (Aqua, 0820 UT). (b) Close-up of helicopter ground track. (c) MODIS-derived sea-ice surface temperature and cloud mask image. (d) NOAA-16 AVHRR-derived ice surface temperature (acquisition time 0832 UT). A NOAA-12 image was also acquired during the flight (not shown; acquisition time 0847 UT). (e) Along-track KT-19.85 skin temperature variations with time, as well as Aqua MODIS, AVHRR NOAA-16 and NOAA-12 values at the track locations. Vertical colored bars show time range of ± 400 s, used in Figure 5 for validation. Note drift in temperature over ice floes in the black KT-19 track due to diurnal temperature change; line fit shown (black) is used in Figure 6 to evaluate diurnal cooling in the MODIS-to-AVHRR comparison.

radiometer data are acquired every ~ 80 m with ~ 65 m diameter averaging. This easily resolves narrow leads (skin temperature of 267–270 K) and thermal gradients across floes. Furthermore, during the period of the flight, the mean surface temperature varies. In the Figure 4e example, the mean temperature of the floe surfaces cools about 7 K during the 95 min flight. To determine the rate of cooling for direct intercomparison of image-derived temperatures, discussed below, we eliminated points with $T > 260$ K and fit a trend line. Warmer temperatures were eliminated because these surfaces are influenced more by the underlying ocean water, and are thus buffered (and so do not show the evening cooling trend).

To compare the narrow, hours-long spot tracks of the helicopter-mounted radiometer with the coarser-resolution, near-instantaneous satellite radiometers, we both smoothed the aerial-based data and narrowed the time window of comparison. Profile data were smoothed by averaging 1.25 km segments of the tracks. We used an 800 s time window centered on the time of satellite image acquisition to reduce the effects of diurnal surface temperature change. These constraints reduced the total number of valid scenes to five AVHRR and four MODIS.

RESULTS AND DISCUSSION

Ship's-rail-mounted validation results

For AVHRR data, 41 overpass periods ('sites') were acquired where skies were clear (less than two-tenths sky cover) and KT-19 data were acquired (Fig. 3a). Skin surface temperatures at the sites ranged from 243 to 269.5 K. Sites over a broad variety of ice types were used, including thick first-year floes,

light nilas and thin smooth floes. Wetted ice or very young thin-ice types were avoided because of the uncertainty of the emissivity and emissivity correction. For MODIS data, 17 sites were identified (Fig. 3b). MODIS sites were fewer because timing of KT-19 acquisitions was set to favor AVHRR overpasses, and three AVHRR sensor platforms were available vs two MODIS platforms.

The relationship between KT-19.82 measurements and the temperature at nearby pixels is highly linear for both sensors. AVHRR data show a high correlation ($r = 0.97$) and a nearly 1 : 1 slope with the ship-board measurements. No differences were seen among the three AVHRR sensors used, validating the separate calibrations of these platforms (the NOAA-12, -15 and -16 AVHRR sensors). For MODIS, the correlation was similarly high ($r = 0.98$), but the data showed a distinct slope and offset. We attribute this to the lower number of sites, and the narrower range of site temperatures, and not to a real effect of the sensor or algorithm. Data for both AVHRR and MODIS fall close to the 1 : 1 line (± 1.0 K for MODIS; ± 1.4 K for AVHRR, 1σ).

Helicopter-mounted validation results

Figure 5 shows ice surface temperature data from the nine satellite images and the corresponding KT-19.85 aerial measurements. Individual scene–radiometer combinations show significant scatter, but the trend for all data is highly linear and almost all lies within 2.5 K of the 1 : 1 relationship (± 1.7 K, 1σ for 236 sites total). We were unable to justify a quantitative linear fit for each of the observation pairs, or for any of the sensors individually. As with the ship's-rail data, scatter in the data is likely due to mixed-pixel and co-registration issues, despite our attempts to reduce these effects.

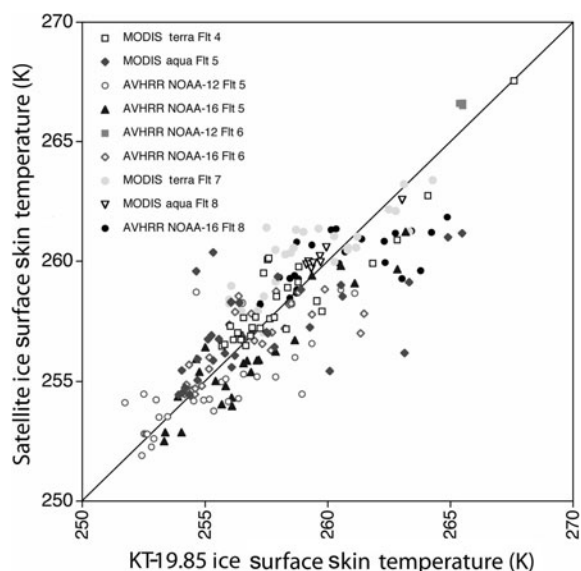


Fig. 5. Helicopter-mounted KT-19.85 ice surface skin temperature vs satellite-derived ice surface temperatures. Each observation set represents 800 s of KT-19 measurements bracketing the time of satellite data acquisition. KT-19 spot measurements are averaged for each 1.25 km of track distance.

Direct comparison of MODIS and AVHRR ice skin temperatures

Figure 6 is a cross-plot of temperature data from the 8 October Aqua MODIS data collection and the NOAA-16 AVHRR data from the same date (see also Fig. 4). The acquisition time for the center of the study region differed by 15 min for the two sensors, 0824 UT for MODIS and 0839 for AVHRR. During this period, significant cooling occurred over the region as local sunset approached. As shown in Figure 4, this trend of cooling was approximately $4.5^{\circ}\text{C h}^{-1}$. However, over thin ice and open water no cooling is observed, because of a buffering effect of relatively warm ocean water.

As implied by that effect, the Figure 6 cross-plot shows a colder trend for the later AVHRR image, but also a steeper slope towards less-cooled thin-ice and open-water temperatures that are thermally buffered by the ocean. To determine the trend in Figure 6, we eliminated those gridcells with temperatures greater than 260 K. This resulted in a highly linear ($r = 0.85$), near-unity (slope = 1.03) relationship between the two products, with a very low mean scatter and standard deviation from the trend (0.68°C and 0.65°C respectively). We consider this to be the best evidence of excellent precision and accuracy in both products. We attribute the observed slope in the trend for the two sensors to be a residual effect of the ocean warming of thinner ice.

Air-temperature inversions and air-temperature–skin-temperature differences

Air temperatures were recorded during all ship's-rail observations by the ARISE cruise meteorological staff. The temperature sensor was located 21 m above the waterline. During the course of the validation experiments, we noted large differences between the KT-19.82 ice surface skin temperature measurements and this air temperature whenever clear-sky and low-wind conditions prevailed (Fig. 7). Temperature differences of $2\text{--}15^{\circ}\text{C}$ were observed, and these

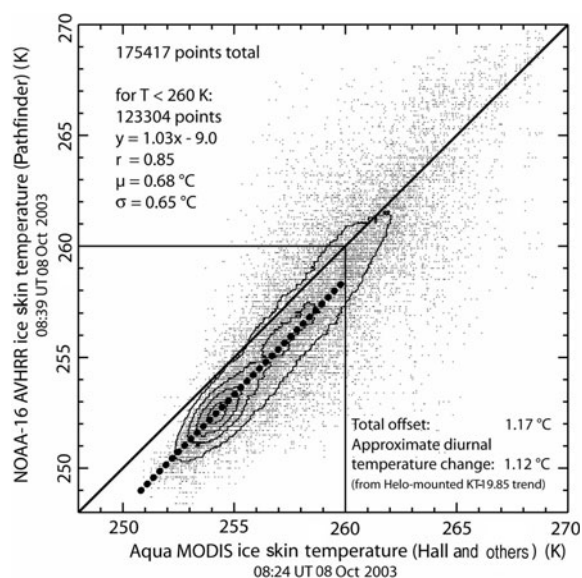


Fig. 6. Cross-plot of clear-sky pixels (using MODIS product cloud mask) from area shown in Figure 4a for both MODIS-derived and AVHRR-derived sea-ice skin temperature during helicopter flight. Contour lines indicate increasing data density near best-fit line. Fit line was determined using only data where $T < 260\text{ K}$ (see text).

formed and decayed rapidly (tens of minutes) as clouds moved into and out of the zenith area. We attribute this to strong atmospheric thermal inversions forming rapidly under clear-sky conditions, and breaking down when clouds covered most of the sky.

Thermal inversions are common polar occurrences; however, these inversions had gradients intense enough (0.25 K m^{-1}) to significantly affect a comparison of meteorological station or automated weather station (AWS) 2 m air temperatures and satellite measurements of ice surface skin temperature. Hall and others (2004) used 2 m air temperatures from South Pole and various Arctic sites in their calibration/validation of the ice surface temperature algorithm, and they observed a consistent offset ($\sim 0.9\text{ K}$) with the satellite value being lower. Moreover, Comiso (2000) and many others attempt to use air temperatures to calibrate surface skin temperature measurements, generally using clear-sky data. This study shows that such comparisons may suffer from this near-surface inversion gradient.

CONCLUSIONS

Our results show that both the AVHRR Polar Pathfinder and MODIS-based ice surface temperature algorithms have highly linear, near-1 : 1 relationships with in situ radiometric measurements. However, in both our validation experiments, mixed-pixel and co-registration effects (particularly difficult issues with sea-ice targets) probably reduce the perceived accuracy of the algorithms below their true levels. Nevertheless, our data show that the satellite-derived products are valid for all ice-type targets over the $245\text{--}270\text{ K}$ range to within at least $\pm 1.5^{\circ}\text{C}$, and probably $\pm 0.7^{\circ}\text{C}$ based on a direct comparison of the two satellite sensors with simultaneous in situ radiometer measurements (Fig. 6). This refines the earlier air-temperature-based validations reported by Hall and others (2004), in their initial discussion of the MODIS-based ice surface temperature algorithm. We further find that near-surface temperature inversions can be strong enough

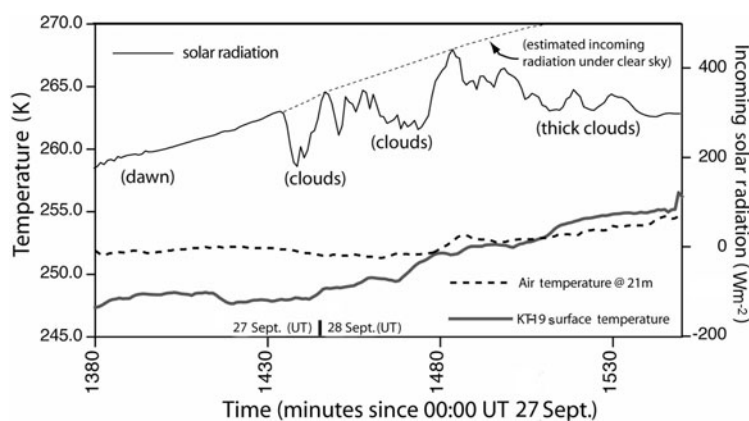


Fig. 7. Air temperatures and sea-ice surface skin temperatures during transition from clear to cloudy periods. Strong surface inversion forms under clear-sky conditions, and breaks down within 15–30 min of cloud cover.

under cold, clear conditions to affect air-temperature–satellite-based ice skin temperature comparisons.

ACKNOWLEDGEMENTS

We acknowledge with gratitude the support of the captain and crew of the *Aurora Australis*. Images and other satellite data required during the cruise were provided by J. Bohlander and J. Smith of NSIDC. Meteorological data were provided by D. Allen, S. Visentin and J. Golding; comparison data from the MAERI ocean/ice radiometric sensing equipment were provided by E. Key and P. Minnett. R.M. was supported by the Australian Government's Cooperative Research Centres Programme through the Antarctic Climate and Ecosystems Cooperative Research Centre (ACE CRC) and ASAC Project 2298. T.S. and T.H. were supported by NASA grant NAG5-11308 and the NASA Snow and Ice Distributed Active Archive at NSIDC.

REFERENCES

- Comiso, J.C. 1994. Surface temperatures in the polar regions from Nimbus 7 temperature humidity infrared radiometer. *J. Geophys. Res.*, **99**(C3), 5181–5200.
- Comiso, J.C. 2000. Variability and trends in Antarctic surface temperatures from in situ and satellite infrared measurements. *J. Climate*, **13**(10), 1674–1696.
- Dozier, J. and S.G. Warren. 1982. Effect of viewing angle on the infrared brightness temperature of snow. *Water Resour. Res.*, **18**(5), 1424–1434.
- Hall, D.K., J. Key, K.A. Casey, G.A. Riggs and D.J. Cavalieri. 2004. Sea ice surface temperature product from MODIS. *IEEE Trans. Geosci. Remote Sens.*, **42**(5), 1076–1087.
- Hastings, D.A. and W.J. Emery. 1992. The Advanced Very High Resolution Radiometer (AVHRR): a brief reference guide. *Photogramm. Eng. Remote Sens.*, **58**(8), 1183–1188.
- Kearns, E.J., J.A. Hanafin, R.H. Evans, P.J. Minnett and O.B. Brown. 2000. An independent assessment of Pathfinder AVHRR Sea Surface Temperature accuracy using the Marine Atmosphere Emitted Radiance Interferometer (MAERI). *Bull. Am. Meteorol. Soc.*, **81**(7), 1525–1536.
- Key, J. and M. Haefliger. 1992. Arctic ice surface temperature retrieval from AVHRR thermal channels. *J. Geophys. Res.*, **97**(D5), 5885–5893.
- Key, J.R., J.B. Collins, C. Fowler and R.S. Stone. 1997. High-latitude surface temperature estimates from thermal satellite data. *Remote Sens. Environ.*, **61**(2), 302–309.
- Lindsay, R.W. and D.A. Rothrock. 1994. Arctic sea ice surface temperature from AVHRR. *J. Climate*, **7**(1), 174–183.
- Maslanik, J., C. Fowler, J. Key, T. Scambos, T. Hutchinson and W. Emery. 1997. AVHRR-based Polar Pathfinder products for modeling applications. *Ann. Glaciol.*, **25**, 388–392.
- Massom, R. and 14 others. 2006. ARISE (Antarctic Remote Ice Sensing Experiment) in the East: validation of satellite-derived sea-ice data products. *Ann. Glaciol.*, **44** (see paper in this volume).
- Minnett, P.J., R.O. Knuteson, F.A. Best, B.J. Osborne, J.A. Hanafin and O.B. Brown. 2001. The Marine–Atmosphere Emitted Radiance Interferometer: a high-accuracy, seagoing infrared spectroradiometer. *J. Atmos. Ocean Tech.*, **18**(6), 994–1013.
- Riggs, G.A., D.K. Hall and S.A. Ackerman. 1999. Sea ice extent and classification mapping with the Moderate Resolution Imaging Spectrometer Airborne Simulator (MAS). *Remote Sens. Environ.*, **68**(2), 152–163.
- Wolfe, R.E. and 6 others. 2002. Achieving sub-pixel geolocation accuracy in support of MODIS land science. *Remote Sens. Environ.*, **83**(1–2), 31–49.